Sensitivity Analysis of Cirrus Cloud Properties from High-Resolution Infrared Spectra. Part I: Methodology and Synthetic Cirrus

Brian H. Kahn

Department of Atmospheric and Oceanic Sciences, University of California, Los Angeles, Los Angeles, California

Annmarie Eldering

Department of Atmospheric and Oceanic Sciences, University of California, Los Angeles, Los Angeles, and Jet Propulsion Laboratory, California Institute of Technology, Pasadena, California

Michael Ghil

Department of Atmospheric and Oceanic Sciences, and Institute of Geophysics and Planetary Physics, University of California, Los Angeles, Los Angeles, California, and Département Terre–Atmosphère–Océan and Laboratoire de Météorologie Dynamique, Ecole Normale Supérieure, Paris, France

Simona Bordoni

Department of Atmospheric and Oceanic Sciences, University of California, Los Angeles, Los Angeles, California

Shepard A. Clough

Atmospheric Environmental Research, Inc., Cambridge, Massachusetts

ABSTRACT

A set of simulated high-resolution infrared (IR) emission spectra of synthetic cirrus clouds is used to perform a sensitivity analysis of top-of-atmosphere (TOA) radiance to cloud parameters. Principal component analysis (PCA) is applied to assess the variability of radiance across the spectrum with respect to microphysical and bulk cloud quantities. These quantities include particle shape, effective radius (r_{eff}), ice water path (IWP), cloud height Z_{cld} and thickness ΔZ_{cld}, and vertical profiles of temperature $T(z)$ and water vapor mixing ratio $w(z)$. It is shown that IWP variations in simulated cloud cover dominate TOA radiance variability. Cloud height and thickness, as well as $T(z)$ variations, also contribute to considerable TOA radiance variability.

The empirical orthogonal functions (EOFs) of radiance variability show both similarities and differences in spectral shape and magnitude of variability when one physical quantity or another is being modified. In certain cases, it is possible to identify the EOF that represents variability with respect to one or more physical quantities. In other instances, similar EOFs result from different sets of physical quantities, emphasizing the need for multiple, independent data sources to retrieve cloud parameters. When analyzing a set of simulated spectra that include joint variations of IWP, r_{eff}, and $w(z)$ across a realistic range of values, the first two EOFs capture approximately 92%–97% and 2%–6% of the total variance, respectively; they reflect the combined effect of IWP and r_{eff}. The third EOF accounts for only 1%–2% of the variance and resembles the EOF from analysis of spectra where only $w(z)$ changes. Sensitivity with respect to particle size increases significantly for r_{eff} several tens of microns or less. For small-particle r_{eff}, the sensitivity with respect to the joint variation of IWP, r_{eff}, and $w(z)$ is well approximated by the sum of the sensitivities with respect to variations in each of three quantities separately.

1. Introduction

Perhaps the greatest uncertainty in predictions of earth's future climate is due to a lack of knowledge about

Corresponding author address: Brian H. Kahn, Dept. of Atmospheric and Oceanic Sciences, University of California, Los Angeles, 405 Hilgard Ave., Box 951565, Los Angeles, CA 90095-1565.
E-mail: kahn@atmos.ucla.edu

clouds, including cirrus, and their interaction with long-wave and shortwave radiation (Houghton et al. 2001). Our ability to quantitatively address the effect of cirrus on the climate system is limited by a lack of observations of cirrus cloud microphysical and bulk properties, such as optical depth (τ), ice water content (IWC), and effective radius (r_{eff}) (Stephens 2002). The sign and magnitude of cirrus cloud net radiative forcing on the

climate system is highly dependent on the values of these properties (Stephens et al. 1990; Fu and Liou 1993). The ice particle habit and shape, and optical properties such as phase function and asymmetry parameter, have been shown to be important for considering the radiative impacts of cirrus as well (Stephens et al. 1990; Liou and Takano 1994).

Infrared (IR) emission spectra are used in identifying and characterizing aspects of the microphysical and optical properties of cirrus clouds. The Infrared Interferometer Spectrometers (IRIS) on *Nimbus-3* (Conrath et al. 1970) and *-4* (Hanel et al. 1972) infrared spectroscopy experiments were utilized for detection of tropical (Prabhakara et al. 1988, 1993) and polar cirrus (Prabhakara et al. 1990). The spectral resolution was fine enough to resolve the IR spectral shape of cloud features, but the footprints were much larger than typical horizontal structures of clouds, at 150 and 95 km for IRIS-B and IRIS-D, respectively. Analysis of more recent measurements from aircraft and ground-based high-resolution infrared spectrometers such as the High Resolution Interferometer Sounder (HIS; Revercomb et al. 1988; Smith et al. 1995) and the Atmospheric Emitted Radiance Interferometer (AERI; Collard et al. 1995) further illuminate the usefulness of high-resolution infrared spectrometry on the detection of cloud properties.

Previously, remote sensing of cirrus cloud properties at IR wavelengths was determined using a particular set of wavelengths. Split-window and trispectral IR techniques use, for instance, 8-, 11-, and 12-μm window channels to exploit the spectral shapes of the indices of refraction for ice and water. Attempts at the differentiation of ice and water clouds (Strabala and Ackerman 1994), identification of coarse categories of cloud morphology (Inoue 1985, 1987), cirrus particle r_{eff} (Ackerman et al. 1990, 1998; Lin and Coakley 1993), contrail r_{eff} (Duda et al. 1998), and even marine stratocumulus r_{eff} (Coakley and Bretherton 1982; Luo et al. 1994) have had considerable success through use of the split-window and trispectral techniques. However, limitations are encountered for retrieval of some microphysical information, such as r_{eff} and shape (Parol et al. 1991) and size distribution (Wu 1987).

Least squares fitting of observed and simulated radiance spectra in the IR window region based on water clouds in the nadir view (Rathke and Fischer 2000) shows some skill in retrieving IR optical depth (τ_{IR}), r_{eff}, and liquid water path (LWP) for clouds with $1 < \tau_{IR} < 4$ when the spectral signatures are strongest, although limitations are encountered for thin and thick clouds outside these values as in Inoue (1985). This technique will probably have more limited use for water clouds in general as τ_{IR} is often higher than this range, but for cirrus there is greater applicability because of the smaller τ_{IR} and stronger spectral shapes usually observed in the radiance spectra. Strong shapes in brightness temperature (T_b) spectra for some cirrus clouds

with τ_{IR} $O(1)$ using radiance observations from the Atmospheric Infrared Sounder (AIRS; Kahn et al. 2003) and IRIS spectra (Prabhakara et al. 1990) support this view.

Over the course of the next several years, there will be a wealth of high-resolution IR emission measurements from several satellite instruments, including AIRS (Aumann et al. 2003) on the Earth Observing System (EOS) *Aqua* satellite, the Tropospheric Emission Spectrometer (TES; Beer et al. 2001), the Infrared Atmospheric Sounding Interferometer (IASI; Simeoni and Singer 1997), as well as the Cross-track Infrared Sounder (CrIS), a part of the future National Polar-orbiting Operational Environmental Satellite System (NPOESS) and NPOESS Preparatory Program (NPP; Cunningham et al. 2004). The AIRS grating spectrometer takes IR spectra for three bandpasses in the 649–2674 cm^{-1} IR range with a scan angle of $\pm$48.95° at a resolving power of $\upsilon/\Delta\upsilon = 1200$ and a circular footprint of 13.5 km at nadir view. CrIS, IASI, and TES will observe the IR spectrum in a similar spectral region as AIRS at a high spectral resolution. There is a need to understand the effect of cloud properties on the broad features (10s to 100s of cm^{-1}) in the radiance of high-resolution IR spectral data from AIRS, CrIS, IASI, and TES, and how these data can be coupled with other cloud observations on the A-train constellation (Stephens et al. 2002), NPP, and NPOESS to retrieve cloud information.

Simulations of downward-looking IR radiance spectra that include cirrus (Bantges et al. 1999; Chung et al. 2000) have been studied as microphysical and bulk cirrus cloud parameters are adjusted separately or together. Bantges et al. (1999) simulated T_b at TOA from 600 to 2500 cm^{-1} for a limited set of microphysical ice models. Chung et al. (2000) investigated simulations produced from a more comprehensive set of physical quantities including r_{eff}, ice water path (IWP), cloud altitude and thickness, multilayering of clouds, and vertical layering of r_{eff}. The results helped to explain the shape of HIS spectra and were most successful for observations containing sloped features in the 800–1000 cm^{-1} window, a feature of cirrus with small r_{eff} (Smith et al. 1998).

When radiance spectra from observational platforms such as AIRS, IASI, and TES are analyzed, the resultant T_b spectra at TOA will reflect the combined effects of a large array of physical quantities. In this work we have asked ourselves the following questions. 1) Which microphysical and bulk cirrus quantities cause the most variability in the brightness temperature at TOA? 2) Does one or more of these quantities dominate the variability? 3) What spectral regions are most sensitive to each quantity? 4) Is it possible to discern the combined effects of several quantities over a set of spectra at TOA, as distinct from the superposition of each effect separately? 5) What is the usefulness of this technique applied to real data and as a cloud characterization tool? 6) Given a level of uncertainty or noise in an instrumental measurement of radiance, does the typical range

of values in a given physical quantity produce variability in the T_b spectra at TOA beyond this level of uncertainty or noise?

The first four questions are addressed in the present paper, which is Part I of a two-part study. The last two questions are addressed in Part II of this work (B. Kahn, A. Eldering, M. Ghil, A. Braverman, and H. Steele, 2004, unpublished manuscript), which will present case studies of AIRS radiances containing cirrus clouds.

2. Methodology

a. Simulations and assumed optical properties

A set of TOA radiance simulations representative of the spectral range for the aforementioned IR emission measurement platforms has been produced with the Code for High Resolution Accelerated Radiative Transfer with Scattering (CHARTS); CHARTS is a plane-parallel, monochromatic radiative transfer model with multiple scattering, which uses the adding–doubling method (Moncet and Clough 1997). The synthetic cirrus cloud extinction and asymmetry parameter spectra were generated by the T-matrix method, where we used randomly oriented cylinders and spheroids at different aspect ratios (Mishchenko and Travis 1998). The spectral characteristics of extinction cross section, single-scattering albedo, and asymmetry parameter for spheroids and cylinders are quite similar to each other, as shown in Mishchenko et al. (1996). Comparisons were made to hexagonal cylinders (Baran et al. 2002) and are similar to circular cylinders and spheroids. Thus, we have chosen to use either monodisperse spheroids or circular cylinders as the scattering media in most of the simulations; the same experiments with different particle shapes yield very similar EOFs. Comparisons of the single-scattering properties for monodisperse and power law size distributions were made, using reasonable values of effective variance (v_{eff}) derived from observed cirrus (Xu et al. 2002). The spectral shapes of the single-scattering properties are similar between the different values of v_{eff}.

The conversion between IWP, r_{eff}, and τ for spheres is well known and straightforward (see McFarquhar and Heymsfield 1998). For circular cylinders the conversion between the same parameters is adopted from Platt and Harshvardhan (1988). As stated in their work, r_{eff} is defined as the following:

$$r_{eff} = \frac{\int_{r_1}^{r_2} r^2 Ln(r)\, dr}{\int_{r_1}^{r_2} Ln(r)\, dr}, \qquad (1)$$

with r as the radius of the cylinder, L the length of the cylinder, and $n(r)$ the number of droplets per unit volume of air at a given radius r. The limits of the integral are taken to be the minimum and maximum size of the particles in the distribution. The ice water content (IWC) of a cylindrical ice particle distribution is

$$IWC = \pi\rho_{ice} \int_{r_1}^{r_2} r^2 Ln(r)\, dr, \qquad (2)$$

where ρ_{ice} is the density of water ice. The ice water path (IWP) of a given cloud is simply IWP = IWC · Δz, where · Δz is the thickness of the cloud. The optical depth (τ) is then defined as

$$\tau = 2\Delta z\zeta \int_{r_1}^{r_2} Q_e r Ln(r)\, dr. \qquad (3)$$

The scalar ζ is a factor introduced by Platt and Harshvardhan (1988) to account for the differences in projected area due to different spatial orientations of the cylindrical particle. In this work, the extinction efficiency (Q_e) is assumed to be 2. For small ice particles at IR wavelengths, this assumption does not strictly hold (see Hansen and Travis 1974), but for the purposes of this sensitivity study the error associated with such an assumption is greatly outweighed by the orders of magnitude variation in IWP and other quantities. To relate IWC and τ to r_{eff}, it follows that

$$r_{eff} = \frac{4\zeta IWP}{\pi\rho_{ice}\tau}. \qquad (4)$$

To generate a reasonable value of ζ over a random orientation of any given cylinder with a fixed aspect ratio, we calculate the projected area as the average for all possible orientations, with each occurring an equal number of times as any other. Taking the ratio of the projected area to $2rL$ produces ζ values of 1.13, 0.97, 0.89, 0.84, 0.81, 0.78, and 0.76 for (prolate) cylindrical aspect ratios of 1.0, 1.5, 2.0, 2.5, 2.86, 3.33, and 4.0, respectively.

We use the index of refraction measurements for water ice determined at 163 K (Toon et al. 1994), which covers the entire spectral region of interest (Massie and Goldman 2003). For simulated radiances there is brightness temperature sensitivity as great as 1–5 K in the atmospheric windows when different values of the index of refraction are used (Kahn et al. 2003). Many of the ice models in this work are highly forward scattering, and we use the delta-M scaling method (see Liou 2002) and the Henyey–Greenstein (1941) scattering phase function. An example set of simulated spectra is shown in Fig. 1. All cloud and atmospheric properties are fixed except for IWP.

In this work, simulations are for the nadir view angle in the 649–1629 cm^{-1} spectral region. Only thermal emission is considered; we will not emphasize the 2169–2674 cm^{-1} region in this work, as it is quite sensitive to reflected solar radiation (see Ackerman et al. 1995). The simulations utilize six different atmospheric profiles that represent a typical (but not comprehensive) global
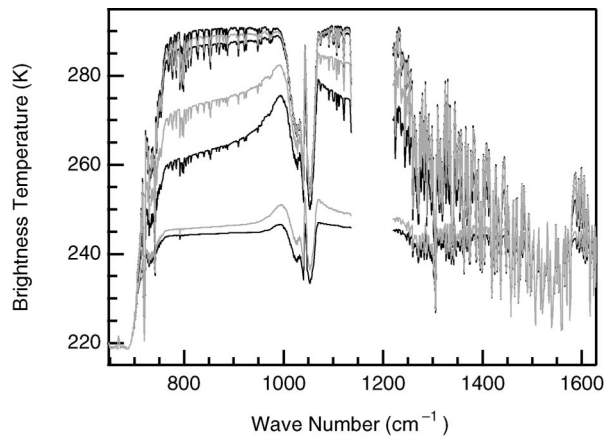
FIG. 1. A set of simulated spectra for IWP values of 10^{-5} (warmest black curve), 5×10^{-5} (warmest gray curve), 10^{-4}, 5×10^{-4}, 10^{-3}, 5×10^{-3} (coolest gray curve), and 10^{-2} g cm^{-2} (coolest black curve), where higher IWP values lead to successively lower T_b values. The cloud is fixed at 6–9 km in a typical middle-latitude summer atmosphere, for monodisperse cylindrical ice particles of 8.0 μm with an aspect ratio of 1.0.

range of $T(z)$ and $w(z)$ over a single day (D. Kinnison 2002, personal communication), shown in Fig. 2. The cirrus clouds are modeled with an assortment of particle shapes and r_{eff}, adjustable thickness ΔZ_{cld} and height Z_{cld}, and a range of IWP. Table 1 describes in detail the range and values of physical quantities used in the simulations, and their groupings in the analysis that will be presented. All simulations have a spectral resolution of 1.5×10^{-4} cm^{-1} and are convolved to 1.0 cm^{-1} (Norton and Beer 1976).

b. Principal component analysis

We use principal component analysis (PCA) to investigate the questions posed at the end of the introduction. In addition to diagnosing TOA IR radiance variability from cirrus microphysical properties (Bantges et al. 1999), PCA has proven useful in verifying radiance spectra derived from general circulation models (GCMs) against TOA radiance observations (Haskins et al. 1997, 1999; Goody et al. 1998; Huang et al. 2002). Huang et al. (2002) showed cloud variability explains the major part of the variation in the University of California, Los Angeles (UCLA), GCM's TOA radiance spectra, although the GCM underrepresents the amount of variability compared to IRIS observations by a factor of 2–6. PCA is also used for the compression and denoising of radiance measurements while maintaining their high information content (Aires et al. 2002), as well as the retrieval of meteorological parameters (Smith and Woolf 1976; Huang and Antonelli 2001; Goldberg et al. 2003). Goldberg et al. (2003) apply PCA to a set of simulated AIRS radiances and indicate that 90% of the variance is explained in the first spectral EOF and nearly 100% in the first ten EOFs.
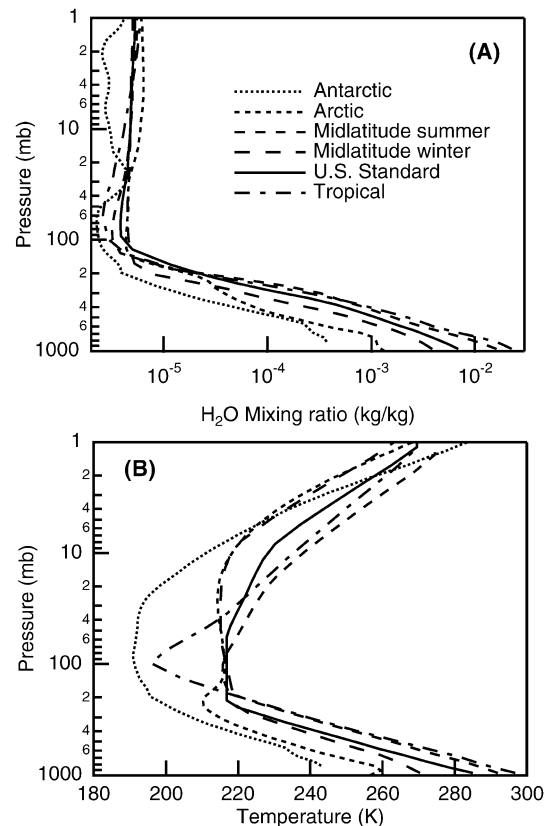

FIG. 2. Profiles of (a) $T(z)$ and (b) $w(z)$ for six different atmospheres used in the radiative transfer simulations. The atmospheres are intended to represent a significant portion of the typical global range in $T(z)$ and $w(z)$ observed for any given day of the year.

In the following, we apply PCA in order to understand the variation in the modeled TOA radiance spectra due to changes in an assortment of microphysical and bulk cirrus cloud parameters and relate the spectral EOFs to these physical quantities.

We start with a number N of synthetic IR spectra, $\{\mathbf{X}^{(n)}: 1 \le n \le N\}$, graphically shown in Fig. 1. Each spectrum is a vector $\mathbf{X}^{(n)} = \{X_{v_1}^{(n)}, \dots, X_{v_k}^{(n)}\}$ with a number K of T_b values as a function of wavenumber v_k. An average spectrum $\overline{\mathbf{X}}$, a function of v_k is calculated from this set of spectra, and $\overline{\mathbf{X}}$ is subtracted from $\mathbf{X}^{(n)}$ in order to generate a perturbation vector $\mathbf{Y}^{(n)}$. The set of N vectors $\mathbf{Y}^{(n)}$ forms the rows of a matrix $\mathbf{Y}$ with dimensions of $N \times K$. The variance–covariance matrix $\mathbf{S}$ is constructed (Wilks 1995) from $\mathbf{Y}$ by

$$\mathbf{S} = \frac{1}{n-1} \mathbf{Y}^{\mathrm{T}} \mathbf{Y}. \qquad (5)$$

Using singular-value decomposition (SVD), an orthonormal basis can be constructed from the eigenvectors of $\mathbf{S}$ (Press et al. 1992). Each eigenvector is known in the meteorological literature (Preisendorfer 1988) as an empirical orthogonal function (EOF); in the present case each EOF $\mathbf{e}^{(m)} = \{e_{v_1}^{(m)}, \dots, e_{v_k}^{(m)}\}$ has K components (in

TABLE 1. List of physical quantities that are adjusted in this work, along with the values used in the CHARTS simulations. Figures associated with each physical quantity (or combinations of physical quantities) are listed on the left.

Physical quantity	Fig.	IWP (g cm^{-2})	r_{eff} (μm)	$T(z)$	$w(z)$	Δz_{cld} (km)	z_{cld} top (km)	Aspect ratio	Particle habit
IWP	3	10^{-2}–10^{-5}	5.0–25.3	MS[a]	MS	3	9	1	Cyl[b]
r_{eff}	4	10^{-2}–10^{-4}	5.0–25.3	MS	MS	3	9	1	Cyl
$w(z)$	5	10^{-2}–10^{-4}	5.0	SA[c]	SA	1	13	1	Cyl
Δz_{cld}	6	5×10^{-3}–5×10^{-5}	5.0, 25.3	MS	MS	1–7	13	1	Sph[d]
z_{cld}	7	5×10^{-3}–5×10^{-5}	5.0–25.3	MS	MS	3	9–14	1	Sph
Aspect ratio	8	10^{-2}–10^{-4}	11.69	MS	MS	3	9	1–5	Cyl
$T(z)$, $w(z)$	9	10^{-2}–10^{-4}	25.3	All[e]	All	3	9	1	Cyl
IWP, r_{eff}	10	10^{-2}–10^{-5}	5.0–25.3	MS	MS	3	9	1	Cyl, Pow[f] Hex[g]
IWP, r_{eff}, $w(z)$	11	10^{-2}–10^{-5}	5.0–25.3	SA	SA	1	13	1	Cyl
IWP, z_{cld}	12	5×10^{-3}–5×10^{-5}	11.69, 25.3	MS	MS	3	9–14	1	Sph

[a] Midlatitude summer atmosphere, for both $T(z)$ and $w(z)$, shown in Fig. 2.
[b] Circular cylindrical ice particles calculated from T-matrix method (Mishchenko and Travis 1998).
[c] Atmospheric $T(z)$ and $w(z)$ taken from Kahn et al. (2003) case study.
[d] Spherical ice particles calculated from T-matrix method (Mishchenko and Travis 1998).
[e] All atmospheric $T(z)$ and $w(z)$ profiles taken from Fig. 2.
[f] Power law size distribution as in Xu et al. (2002).
[g] Hexagonal cylinders calculated by Baran et al. (2002).

kelvins). The eigenvalue λ that corresponds to a given EOF is equal to the variance in the data associated with that EOF; the sum of the eigenvalues of **S** equals the total variance of the dataset. The relative variance associated with the mth EOF, $1 \leq m \leq K$, is given by

$$\sigma_m^2 = \frac{\lambda_m}{\sum_{i=1}^{K} \lambda_i}. \tag{6}$$

We are interested in the spectral sensitivity due to the assorted cloud properties, where the spectral EOFs show the range of wavenumbers where the sensitivity is relatively strong or weak.

Our purpose is to determine the extent to which a particular EOF may be attributed to a physical parameter (for instance, IWP, r_{eff}, aspect ratio, etc.) or a unique combination of parameters. An EOF analysis on N simulations for a single physical quantity will be performed, and the EOFs can be compared to EOFs that result from an analysis of a simulation set in which multiple physical quantities are varied.

In order to see the relative importance of each EOF for a given synthetic perturbation spectrum $\mathbf{Y}^{(n)}$, the PCs $\mathbf{a}^{(j)} = \{a_1^{(j)}, \ldots, a_N^{(j)}\}$, $1 \leq j \leq N$, are calculated by

$$a_n^{(j)} = \sum_{k=1}^{K} e_{v_k}^{(j)} Y_{v_k}^{(n)}. \tag{7}$$

In this work, we concentrate on the leading M EOFs, $M < K$; M is determined by the requirement that $\sum_{i=1}^{M} \lambda_i$ equal 99% or more of the total variance. Equation (7) yields the PCs by projecting the original synthetic spectra onto each EOF. A single PC shows the contribution of the corresponding EOF to reproducing the original spectrum $\mathbf{Y}^{(n)}$; $\mathbf{Y}^{(n)}$ can be recalculated from its associated set of $a_m^{(n)}$ and the set of EOFs $\mathbf{e}^{(m)}$ by

$$Y_{v_k}^{(n)} = \sum_{j=1}^{N} a_n^{(j)} e_{v_k}^{(j)}. \tag{8}$$

The EOFs are often normalized to unit length so that the sum of the squares of the elements of $\mathbf{e}^{(m)}$ sum to unity (in nondimensional units). We have chosen here, instead, to scale the EOFs by $\lambda^{1/2}$ to show the relative importance of each EOF compared to the others; this ensures that the PCs are appropriately scaled. We will use the PCs only in Part II, to map out the horizontal spatial patterns associated with a given EOF. Thus, the PC map should resemble to an extent the particular physical quantity in the observed field to which the spectra are most sensitive.

3. Results

Here we expand on the work of Bantges et al. (1999) and Chung et al. (2000) and use PCA to diagnose the cloud microphysical and bulk properties most responsible for the variance seen in simulated high-resolution IR spectra. The parameters that have been studied include r_{eff}, aspect ratio, $T(z)$, $w(z)$, ΔZ_{cld}, Z_{cld}, and IWP. For most of the following individual parameters, the associated variance of EOF-1 is close to, but not equal to, 100% of the total variance. For simulations with multiple varying parameters, several EOFs have enough associated variance to be considered important.

In the following subsections, we have organized the PCA results into two parts: EOFs based on adjustment of individual and, then, multiple physical quantities. It is important to note that when simulations in multiple parameter space are performed, all possible combinations are used only once. For instance, if 10 values each of IWP, r_{eff}, and $w(z)$ are modeled simultaneously, there will be 1000 spectra to consider in the PCA.
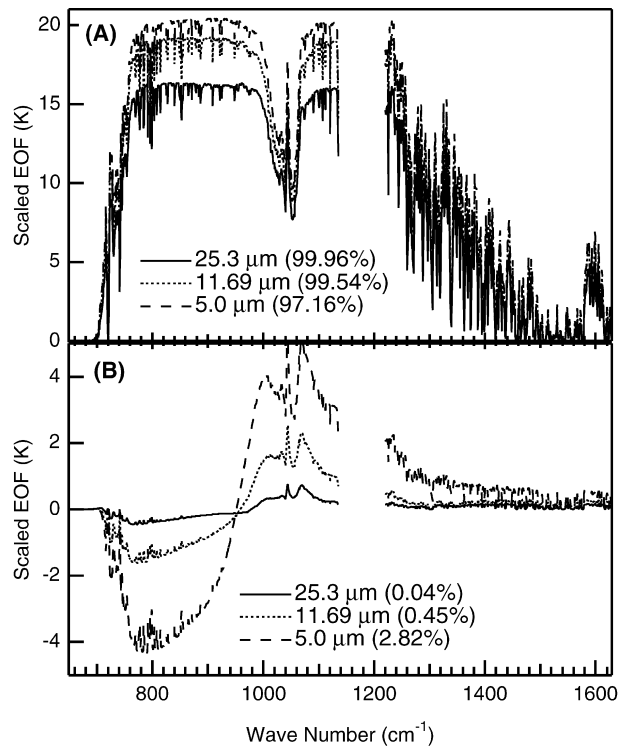
FIG. 3. (a) Scaled EOF-1 for IWP variation in a middle-latitude summer atmosphere at three r_{eff} for monodisperse ice cylinders. and (b) EOF-2. The IWP values are 10^{-2}, 10^{-3}, 10^{-4}, and 10^{-5} g cm^{-2}. The cirrus cloud is placed at 6–9 km. Associated variance is in parentheses.

a. Single parameters

It is expected that a group of footprints for observed high-resolution IR spectra will capture ranges of values for several physical quantities simultaneously. The variance in the EOFs produced by each individual physical quantity does not uniquely impact specific spectral regions in the IR. Thus, simulations where multiple physical quantities vary are thought to be more realistic, although EOFs of simulations where only single quantities vary are useful in interpreting the spectral shapes of EOFs from multiple parameter spaces. In the single parameter space, we show only the leading two EOFs, as these explain almost 100% of the total variance (within a few tenths of a percent or less) in all cases we investigated.

1) ICE WATER PATH

The variation in T_b spectra at TOA due to sensitivity in τ is closely related to sensitivity in IWP. All simulations using CHARTS have τ as an input parameter and are then converted to IWP. Discussion on the assumed relationships among IWP, τ, and r_{eff} are found in the methodology, section 2.

Figure 3 shows both EOF-1 and EOF-2 for three sets of simulations, where r_{eff} is fixed and IWP is changed,

using the midlatitude summer atmosphere, shown in Fig. 2. The same IWP simulations in Fig. 2 for other atmospheres (not shown) represent the same general behavior as indicated by the midlatitude summer case; $T(z)$ in each atmosphere determines the contrast between the cloud temperature T_{cld} and surface temperature T_{sfc}, which then determines the magnitude of variability in the EOFs. A larger contrast between T_{cld} and T_{sfc} results in a greater variability, and vice versa. As seen in Fig. 3, EOF-1 has the most variability in the atmospheric windows, with reduced or no variability near the centers of the H_2O ν_2 vibrational–rotational band centered at 1595 cm^{-1}, the CO_2 ν_2 vibrational band centered at 667 cm^{-1}, and the O_3 ν_3 vibrational band centered at 1043 cm^{-1}. For the three different r_{eff} experiments shown, the shape of EOF-1 shows little change but scales up or down; however, the variance increases with smaller r_{eff}, as with EOF-2. This is consistent with the spectral shape in the atmospheric windows; as the particle gets smaller, the magnitude of the slope and curvature increase greatly. The overall magnitude of the EOFs for changing IWP will increase as the contrast between T_{cld} and T_{sfc} increases, the effects of which are shown in the Z_{cld} case, discussed later.

2) PARTICLE SIZE r_{eff}

In an atmosphere where r_{eff} is varied with all other parameters fixed, the spectral sensitivity is a strong function of the IWP. Figure 4 shows when r_{eff} is changed for three different experiments with fixed IWP values, the entire spectrum of EOF-1 shifts up or down. Additionally, the dominant variability is within the 800–1000 cm^{-1} window for moderate IWP. As IWP is increased to a higher or lower value, the amount of variation in the T_b spectra decreases markedly. For a high IWP, the variability becomes very similar across both windows either side of the O_3 band. As with IWP variations, the magnitude of the EOFs will increase (decrease) as the contrast between T_{cld} and T_{sfc} increases (decreases). Thus, the largest magnitude of EOF variability is seen for clouds with moderate IWP near the tropopause in an atmosphere with large T_{cld} and T_{sfc} differences.

3) WATER VAPOR $w(z)$

The spectral variability due to $w(z)$ changes alone occurs most strongly near the center of the H_2O vapor band, as seen in Fig. 5. This particular example was generated using the South American $T(z)$ and $w(z)$ profiles, used in Kahn et al. (2003), for a cloud fixed at 12–13 km with a monodisperse spherical particle model of 5.0 μm. Some variability also occurs in the atmospheric window, a signature of the water vapor continuum. In both EOF-1 and EOF-2 the greatest variability in the 800–1000 cm^{-1} window occurs closer to 800 cm^{-1} where the water vapor continuum has a stronger
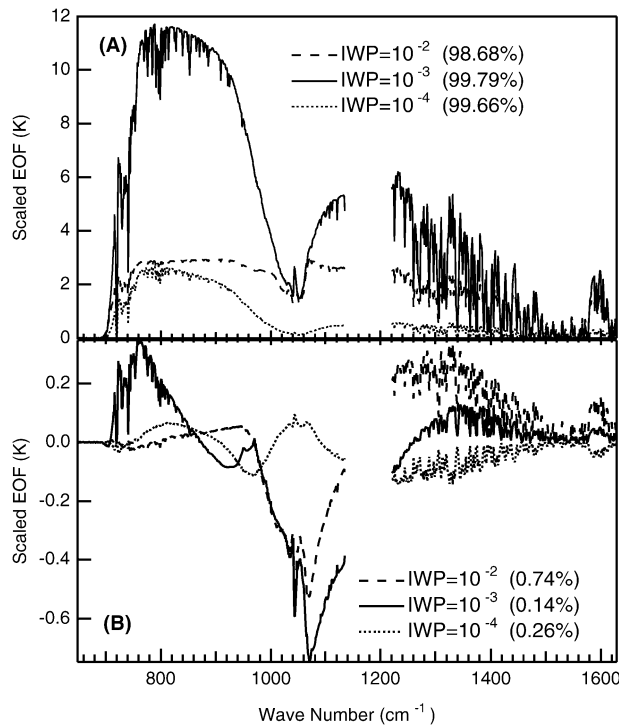
FIG. 4. (a) EOF-1 for variable r_{eff} (using simulations at 5.0, 8.0, 11.69, 16.0, 21.0, and 25.3 μm) for three separate experiments for different and fixed IWP values (g cm^{-2}). (b) As in (a) but for EOF-2. The cylindrical ice cloud with aspect ratio of 1.0 is fixed in height from 6 to 9 km in a middle-latitude summer atmosphere.
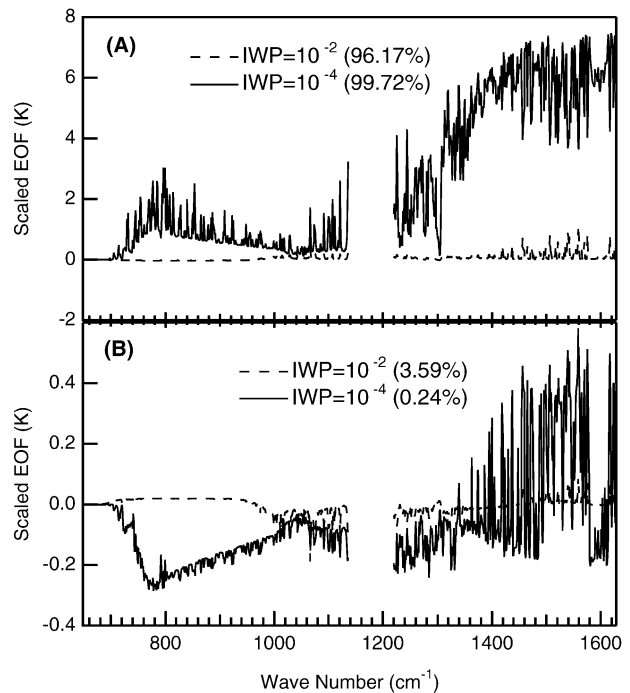
FIG. 5. Variation of $w(z)$ for a fixed atmospheric profile using the South American Andes case used in Kahn et al. (2003). Particle r_{eff} is constant at 5.0 μm for monodisperse cylindrical ice particles with aspect ratios of 1.0. The cloud is fixed at 12–13 km for two cases: an IWP of 10^{-2} and 10^{-4} g cm^{-2}. The entire H_2O vertical mixing ratio profile is scaled by 0.4, 0.6, 0.8, 1.2, 1.4, and 1.6 to generate the $w(z)$ variability: (a) EOF-1 and (b) EOF-2. Associated variance is in parentheses.

effect on the attenuation of upward radiance. When the IWP values are relatively low, the water vapor (which is concentrated below the cloud) shows up clearly because the effect of H_2O on the upwelling radiance can be sensed above the cloud. For the case of an optically thick cloud, the amount of spectral variability is very small because of the lack of water vapor above the cloud. These spectral features are seen in the EOFs presented by Aires et al. (2002), where PCA was applied to 2311 real atmospheric profiles spanning a large range of vertical profile shapes in $T(z)$ and $w(z)$.

4) CLOUD THICKNESS ΔZ_{cld}

For simulations with a midlatitude summer atmosphere and cloud thickness varied in 1-km increments, Fig. 6 shows the EOF variability across a range of IWP values with a fixed cloud top at 13 km and variable base from 6 to 12 km. In an atmosphere with low IWP, the greatest variance is seen in the 800–1000 cm^{-1} window, with a secondary maximum in the center of the broad region of H_2O absorption centered near 1600 cm^{-1}. However, the overall variation is small for such a thin cloud. The relatively larger magnitude of variation seen in the H_2O region is attributable to the vertical distribution of the IWC. When the cloud is very disperse (6–

13 km), the absorption lines due to H_2O are much more easily seen in the EOF than in the case where the cloud geometrical thickness is 1 km because radiance from the lower portions of the cloud makes it to higher levels more easily. When the IWP values are moderate, the spectral variability resembles that of the low IWP case except the magnitude of variance is much higher. When IWP is increased to a high value, the variability is drastically different and resembles the shape of the extinction spectrum for the particular ice model used. There are differences in the spectral shapes between different particle sizes (not shown). For smaller particle sizes, the spectral slopes are steeper than larger sizes. With a realistic size distribution, as opposed to monodisperse sizes, some of the sharp features smooth out. In the case where cloud base is fixed to 6 km and cloud top is adjusted from 7 to 13 km, it resembles closely the case of Z_{cld}, discussed below.

5) CLOUD HEIGHT Z_{cld}

Figure 7 shows an atmosphere where Z_{cld} is adjusted with ΔZ_{cld} and all other parameters fixed. The behavior of the EOFs for the low IWP experiment is very similar to that in the case for low IWP with a range of ΔZ_{cld}.
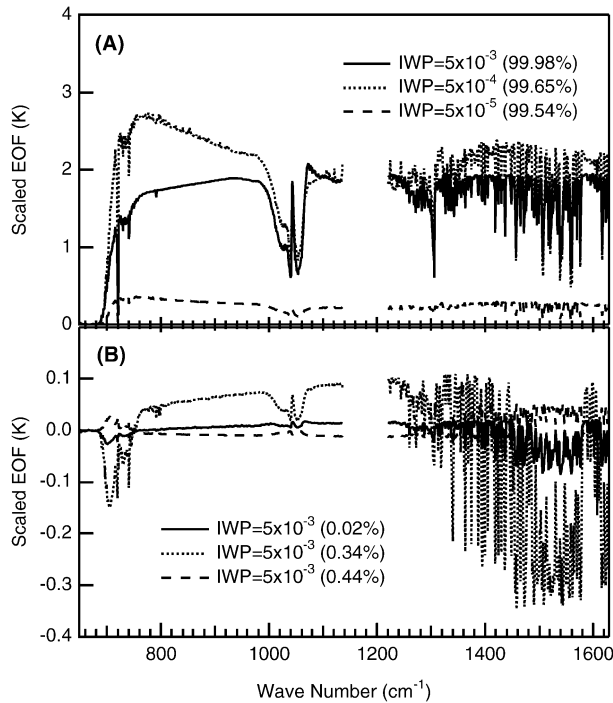
FIG. 6. (a) EOF-1 for variation of cloud thickness (ΔZ_{cld}) in a middle-latitude summer atmosphere. The set of simulated radiances is generated by varying the lower cloud boundary from 6 to 12 km, while fixing the top at 13 km. (b) As in (a) except for EOF-2. All results are for spherical monodisperse particles with r_{eff} of 25.3 μm for three experiments: fixed IWP values at 5×10^{-3}, 5×10^{-4}, and 5×10^{-5} g cm^{-2}. Associated variance is in parentheses.

FIG. 7. (a) EOF-1 for variation of cloud height Z_{cld}. The cloud thickness is fixed to 3 km, and the base (top) is varied from 6 to 11 (9 to 14) km in a middle-latitude summer atmosphere. (b) As in (a) except for EOF-2. The ice model used is a monodisperse ice sphere with r_{eff} of 5.0 μm. Associated variance is in parentheses.

The same arguments about H_2O vapor absorption in the ΔZ_{cld} case probably explain why there is a large magnitude of variability in the middle of the H_2O region compared to the adjoining windows. The degree of variability in the EOFs is about twice that of the EOFs from ΔZ_{cld}, however. At a moderate IWP value, the variability increases greatly throughout the entire spectral region including the H_2O region, except near the CO_2 band. When the cloud is more opaque and is moved vertically, the outgoing radiance does not penetrate the cloud. Thus, there is more variability from simulated spectrum to spectrum as cloud height is increased, leading to a larger magnitude of variability in EOF-1. This effect is at a maximum when IWP values are largest.

6) ASPECT RATIO

Figure 8 shows the two leading EOFs of aspect ratio changes of prolate cylinders with r_{eff} of 11.69 μm. Experiments for oblate cylinders (spherical disks), as well as prolate and oblate spheroids yield nearly identical EOFs; no other shapes were considered here. An important feature is that the shape of EOF-1 is not preserved as IWP and r_{eff} (other sizes not shown) are adjusted independently. Therefore, in order to obtain such
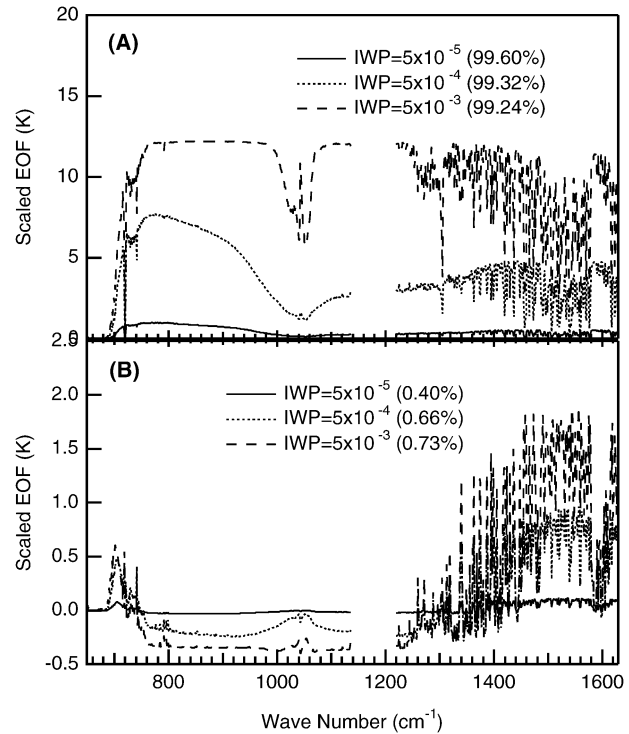
an EOF in observed IR spectra, r_{eff} and IWP must be relatively homogeneous over the entire cloud scene analyzed. Additionally, and r_{eff} distribution will flatten out the spectral shape from aspect ratio differences. The aspect ratio must be relatively homogeneous within each footprint in the cloud scene and must vary from spectrum to spectrum (footprint to footprint) substantially enough in order for the shape to appear in the EOF. Real cirrus clouds are generally composed of homogeneous mixtures of particles of different sizes, shapes, and habits in volumes much smaller in size by many orders of magnitude than the volume of atmosphere represented in the horizontal scale of an AIRS footprint. The expectation of such idealized requirements on a regular basis, if at all, is unrealistic. Further, the maximum sensitivity occurs for τ_{IR} on the order of 1, and this sensitivity is markedly reduced at lower and higher values. Bantges et al. (1999) pointed out the 2400–2500 cm^{-1} spectral bandpass may be useful for retrieving information on aspect ratio. In Fig. 8 we have shown a feature similar to what Bantges et al. (1999) described: the sloped T_b spectrum from 2400 to 2500 cm^{-1}. This sort of feature is expected to be very difficult to observe at best; in typical cirrus clouds the fundamental heterogeneity of IWP, r_{eff}, shape, and habit should obscure any aspect ratio signature in nearly all circumstances, at least over the horizontal scale of an AIRS footprint.
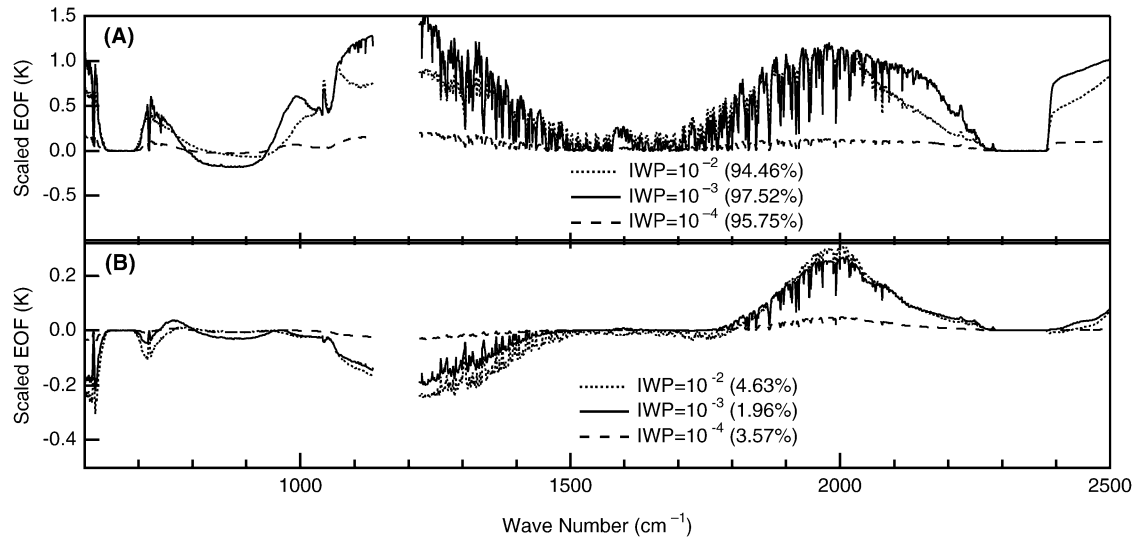
FIG. 8. (a) EOF-1 for variations in aspect ratio of monodisperse prolate cylinders with r_{eff} of 11.69 μm. for three different experiments at fixed IWP values. The values used for aspect ratio variability are 1.0, 1.5, 2.0, 2.5, 2.86, 3.33, and 4.0. (b) As in (a) except for EOF-2. Cloud height is fixed at 6–9 km in a middle-latitude summer atmosphere. Associated variance is in parentheses.

b. Multiple parameters

We will now look at multiple parameter spaces. Sets of simulated TOA radiances where ranges in the values of multiple parameters are changed and simulated, and PCA is applied to the sets of spectra. EOFs derived from these spectra will be compared to the EOFs presented in section 3a, where similarities and differences in the spectral shape and magnitude of variability of the EOFs will be highlighted.

1) TEMPERATURE $T(z)$ AND MIXING RATIO $w(z)$

Experiments are performed to see the response of T_b spectra at TOA to simultaneous changes in the profiles of $T(z)$ and $w(z)$. In Fig. 9, the three leading EOFs are shown for the range of $T(z)$ and $w(z)$ presented in Fig. 2 at two different fixed IWP values. EOF-1 is nonzero everywhere because $T(z)$ and $w(z)$ differences between the atmospheres will appear in the CO_2, O_3, and H_2O bands. The largest variation is seen in the atmospheric windows where interference due to gas is minimal. The variation in the H_2O band is greatest for the highest IWP value. EOF-2 and EOF-3 indicate additional variance in the O_3, H_2O, and CO_2 bands with more subtle differences between the different IWP cases. If the results are compared with those of Fig. 5, where the only physical quantity adjusted is $w(z)$, it is clear that changes in $T(z)$ dominate greatly over changes in $w(z)$ for the atmospheres in Fig. 2. In the analysis of observational data, these sorts of signatures are expected to manifest themselves in regions with large thermal and moisture gradients, such as those found near frontal systems, or near the coastal regions of landmasses. In more localized

regions, the variability of $T(z)$ is much less and the magnitude of EOF-1 is smaller. As with the $w(z)$ case alone, the spectral features associated with $T(z)$ variability are seen in the EOFs presented by Aires et al. (2002).

2) IWP AND r_{eff}

Figure 10 shows the leading two EOFs when IWP and r_{eff} vary simultaneously for three different experiments: circular and hexagonal cylinders and a power distribution of spheres with an effective variance (v_{eff}) of 0.05. A comparison with Fig. 3, which shows EOFs for IWP variations alone, shows that the leading two EOFs of Fig. 3 have the same shape as the leading two EOFs of Fig. 10. This is true for the assortment of fixed r_{eff} in Fig. 3. If the highest IWP value or two is removed, the shape of EOF-1 takes on a more rounded appearance than in Fig. 3 (not shown). The magnitude of EOF-2 may be useful for information on the average r_{eff} for a set of measurements. If IWP changes occur in cirrus clouds with small r_{eff}, the associated variance of EOF-2 is greater than in a comparable cirrus cloud with larger r_{eff}. Successive EOFs beyond EOF-1 and EOF-2 are different in shape when IWP and r_{eff} are changed jointly compared to the case where IWP alone is changed, although the amount of variance is low for such EOFs; it is uncertain they would appear distinct from variations of other physical quantities. The differences in the shape of the EOFs between the different models are quite small, with the greatest differences for EOF-2 in the 1000–1250 cm^{-1} region; this coincides with the spectral region where differences in extinction show up most
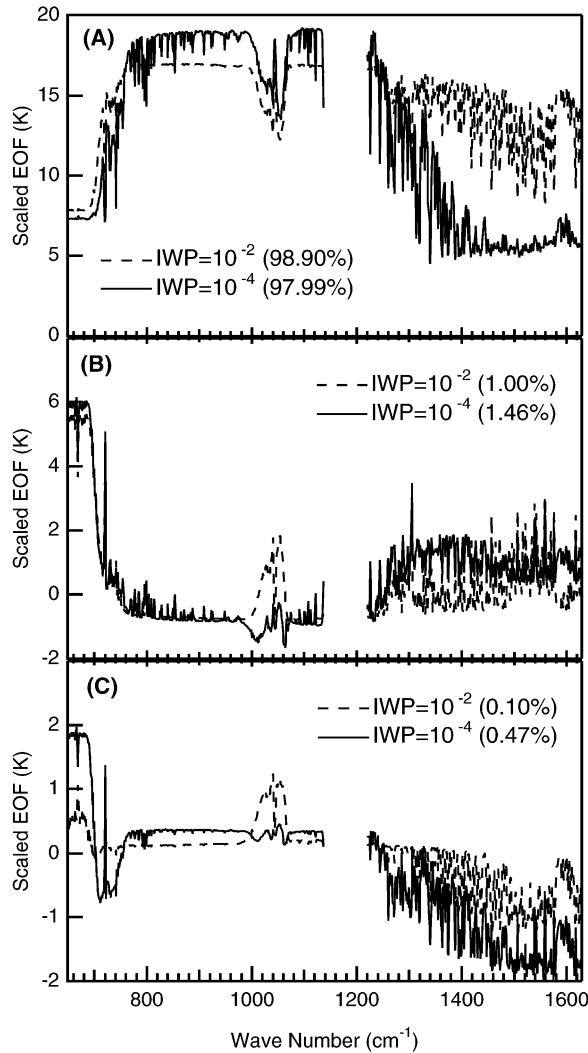
FIG. 9. (a) EOF-1 for a variable atmosphere: both $T(z)$ and $w(z)$ are varied. with all other gas profiles fixed. Atmospheres used are shown in Fig. 2. Shown are the EOFs for two experiments with IWP values of 10^{-2} and 10^{-4}. Both (b) and (c) as in (a) except for EOF-2 and EOF-3, respectively. Particle size is held at 25.3 μm; the cloud is located between 6 and 9 km; and cylindrical ice particles with an aspect ratio of 1.0 are used.
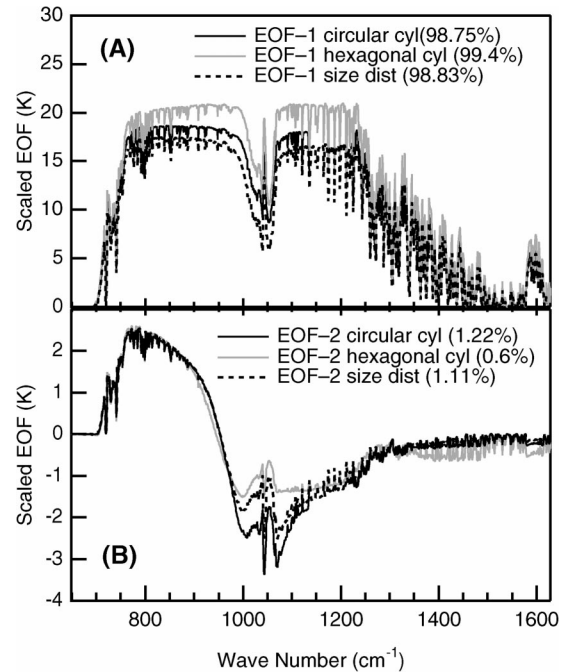

FIG. 10. Size and IWP varied simultaneously in a middle-latitude summer atmosphere for three different experiments: monodisperse cylinders with an aspect ratio of 1.0, hexagonal cylinders as given by Baran et al. (2002), and a power law size distribution of spheres with effective variance (v_{eff}) set to 0.05: (a) EOF-1 and (b) EOF-2. The cloud is fixed to 6–9 km. For the circular cylinders, the 24 simulated radiances are formed by combinations of the following: IWPs of 10^{-2}, 10^{-3}, 10^{-4}, and 10^{-5} g cm^{-2}, and r_{eff} of 5.0, 8.0, 11.69, 16.0, 21.0, and 25.3 μm. For the hexagonal cylinders, a similar IWP range is used, and the hexagonal column length values are [see Baran et al. (2002) for assumed aspect ratios] 7.5, 15, 25, 35, 45, 60, and 80 μm. For size distribution we assume the same r_{eff} as the monodisperse experiment, and a similar range in IWP.

prominently between the models. The shape of EOF-1 is very similar with a slight difference in BT slope in the atmospheric windows. The offset in magnitude is related to slightly different ranges in values used for IWP.

3) IWP, r_{eff}, AND $w(z)$

Figure 11 shows the three leading EOFs for joint variation in the values of IWP, r_{eff}, and $w(z)$. EOF-1 and EOF-2 resemble the results for joint IWP and r_{eff}, shown in Fig. 10. The rounded appearance in the 770–1000 cm^{-1} window in EOF-1 indicates the presence of small-

er r_{eff}. Additionally, EOF-2 resembles EOF-2 in Fig. 10. In Fig. 11, the two IWP experiments indicate IWP across a full range of values (IWP-1), and for a range where the highest values are removed (IWP-2), in order to represent a set of thinner clouds. For experiment IWP-2, the amount of variation in both EOF-1 and EOF-2 is reduced compared to experiment IWP-1. This is expected because more radiance will pass through the cloud in low IWP cases, leading to less variation in T_b from spectrum to spectrum. EOF-3 shows the signature of water vapor with increased variance in the H_2O vapor band and less in the CO_2 and O_3 bands. One difference between EOF-3 in Fig. 11 and EOF-1 in Fig. 5, which shows results for $w(z)$ sensitivity, is the presence of some negative values near the O_3 band and in the 1050–1250 cm^{-1} window. Thus, it appears that EOF-3 is not only representative of $w(z)$; some of the variance produced by IWP and r_{eff} contributes to the shape of EOF-3. Also, $w(z)$ could be contributing to some of the variability of EOF-1 and EOF-2. However, EOF-3 is clearly indicating there is $w(z)$ sensitivity, as it closely resembles EOF-1 of Fig. 5, with the largest variance occurring
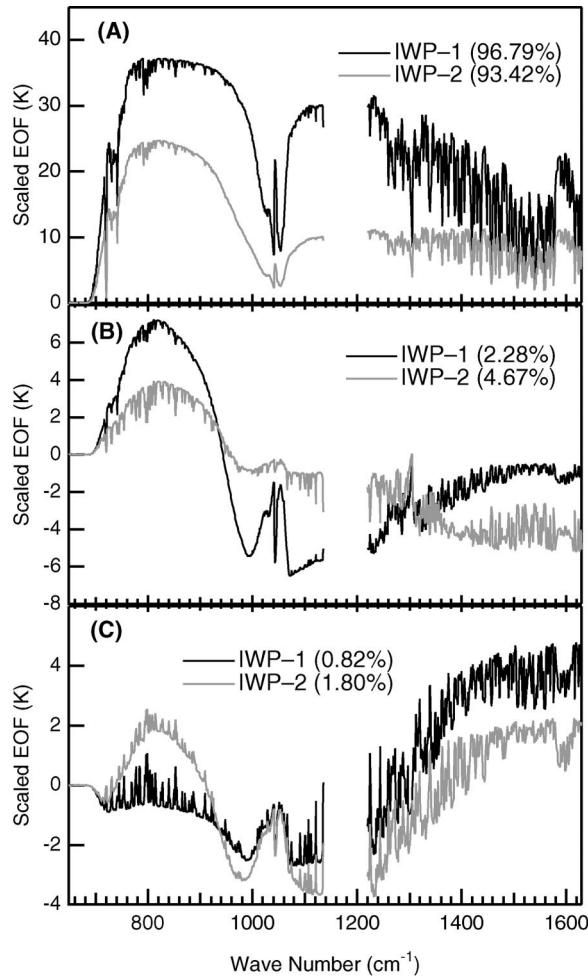
FIG. 11. (a) EOF-1 for the variation of IWP, H_2O vapor, and r_{eff} simultaneously using an NCEP AVN model atmosphere of $T(z)$ and $w(z)$ and single-scattering parameters as given in Kahn et al. (2003). Both (b) and (c) as in (a) except for EOF-2 and EOF-3, respectively. The AVN $w(z)$ profile is scaled by factors of 0.4, 0.6, 0.8, 1.2, 1.4, and 1.6. Increments of IWP include 10^{-5}, 5×10^{-5}, 10^{-4}, 5×10^{-4}, 10^{-3}, 5×10^{-3}, and 10^{-2} g cm^{-2}. Particle sizes are 5.0, 8.0, 11.69, 16.0, 21.0, and 25.3 μm. The experiment IWP-1 includes all IWP values aforementioned; IWP-2 includes all but 10^{-2} and 5×10^{-3} g cm^{-2}; hence, is representative of thinner clouds.
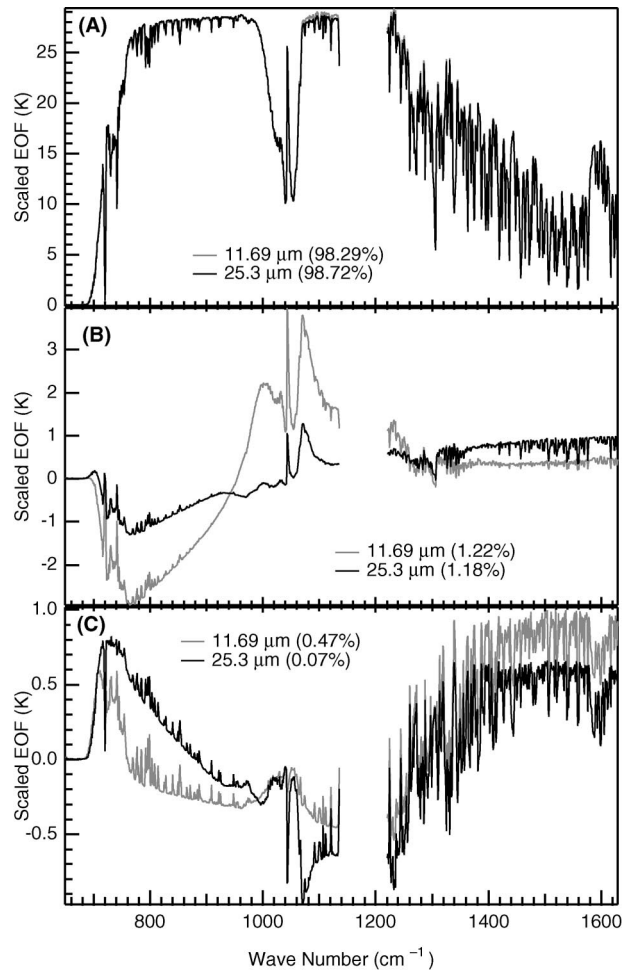
FIG. 12. (a) Leading EOF for the simultaneous variation of IWP and cloud height in a middle-latitude summer atmosphere for two fixed particle sizes of 11.69 and 25.3 μm. The cloud thickness is fixed to 3 km, the base (top) is varied from 6 to 11 (9 to 14) km, and the IWP values are 5×10^{-5}, 5×10^{-4}, and 5×10^{-3} g cm^{-2}: (b) and (c) for EOF-2 and EOF-3, respectively.

in the H_2O band. Thus, it has been shown in this example that $w(z)$ sensitivity is observed in a separate EOF from IWP and r_{eff} sensitivity, as long as the range of values in $w(z)$ is large enough to produce a significant enough amount of variability in the radiance spectra.

4) CLOUD HEIGHT Z_{cld} AND IWP

Figure 12 shows the leading three EOFs for joint Z_{cld} and IWP variations. There are some striking similarities between Figs. 11 and 12: EOF-1 explains most of the variance and resembles IWP sensitivity, EOF-2 resembles a secondary EOF of IWP in the presence of small r_{eff}, and EOF-3 resembles a shape indicative of $w(z)$

sensitivity. In the case of Fig. 11, $w(z)$ is varied; in Fig. 12, $w(z)$ is fixed. Due to the vertical placement of the cloud, the T_b at TOA is sensitive to the amount of H_2O vapor above the cloud, which varies according to the height, as discussed in section 3a. Thus, it is possible to misinterpret EOF results of real data without some a priori knowledge of Z_{cld} and horizontal variations of $w(z)$. There are different combinations of physical quantities that can produce similar EOFs when compared to each other, as is seen in Figs. 11 and 12. For instance, use of independent data sources to better define the cloud boundaries would assist in better interpretation of such EOFs derived from observational IR radiance spectra, as quantified by Cooper et al. (2003).

4. Other physical quantities

There are other physical quantities that have been considered in addition to those already presented. Prab-

hakara et al. (1990) and Chung et al. (2000) show results for vertical r_{eff} stratification experiments. The difference in T_b among the different vertical r_{eff} configurations for both studies is on the order of a few kelvins in the atmospheric windows. Thus, the potential for one or more EOFs with distinct features of vertical stratification manifesting itself in observed spectra on a regular basis seems low for two reasons: 1) the same arguments about horizontal heterogeneity and aspect ratio also apply to vertical stratification and 2) the greatest sensitivity occurs in the window regions where IWP, cloud height and thickness, and r_{eff} are highly sensitive. A similar argument can be applied to particle size distribution effects as well. The results presented earlier for simultaneous r_{eff} and IWP variations indicate little sensitivity in the EOFs from changes in size distribution characteristics. However, subtle changes in the shape of EOFs for different assumed size distributions presented here can lead to retrieval errors in r_{eff}, especially for the larger particle sizes (Fu and Sun 2001).

Yang et al. (2003) present examples of simulated cloud IR radiances in the spectral regions of interest where the addition of a small amount of LWC to the total water content (TWC) causes significant changes in the shape and characteristics of the radiance spectra. Further exploration of mixed phase clouds should be considered. Multilayered clouds also impact the shape of radiance spectra, which can be considered as a combination of the vertical stratification and mixed phase problems. Footprints partially filled with cloud also cause a T_b slope in the atmospheric windows (Coakley and Bretherton 1982; Luo et al. 1994). Additionally, aerosols can contribute to spectral shape, with larger contributions from heavy aerosol loading events such as biomass burning, dust storms, and industrial activity.

5. Discussion and conclusions

The primary goal of this work is to quantify the spectral variability for collections of simulated high-resolution IR spectra. In our analysis, we investigated ranges in the quantities of cirrus cloud and atmospheric properties such as IWP, aspect ratio, r_{eff}, $w(z)$, Z_{cld}, ΔZ_{cld}, and $T(z)$ are adjusted separately or simultaneously. Principal component analysis (PCA) was used to ascertain the variability in the shape and magnitude of the simulated spectra due to the sensitivity of these physical quantities. The variability is investigated for individual physical quantities and for assorted combinations.

The microphysical and bulk cirrus quantities that cause the most variability in the brightness temperature at TOA are IWP, Z_{cld}, ΔZ_{cld}, and $T(z)$. On localized spatial scales, IWP appears to dominate the variability, based on analysis of AIRS data to be presented in Part II. However, it is important to emphasize that spectral variability changes from one range of values for a given physical parameter to another; the range of values may be different from location to location or from time to

time. Therefore the particular spatial domain chosen for PCA may affect the results of the sensitivity analysis as applied to real data. Simulations show that additional significant contributions to spectral variability arise from $w(z)$ and r_{eff}.

Other physical quantities that contribute small shape and variability in limited instances are size distribution and vertical stratification of r_{eff}, as well as particle shape and habit. The primary reason for these contributions being small is the fundamental heterogeneity of cirrus clouds at the scale of an AIRS footprint. Further, the EOFs of aspect ratio undergo significant changes in shape for different IWP and r_{eff}; therefore, this behavior implies that there is no single, unique EOF attributable to aspect ratio. Even if such arguments do not always apply, the sensitivity of the simulated IR radiances to physical quantities such as IWP, Z_{cld}, ΔZ_{cld}, $T(z)$, $w(z)$, and r_{eff} dominate greatly over size distribution and vertical stratification of r_{eff}, as well as particle shape and habit sensitivity, in the same spectral regions.

By applying PCA to simulated radiances, we have shown that it is sometimes possible to discern the combined effects of several quantities over a set of spectra at TOA, as distinct from each effect individually. For small-particle r_{eff}, the EOFs that result for joint variations in IWP, r_{eff}, and $w(z)$ are approximated by the superposition of the EOFs obtained from analysis of simulations in which we vary each of three quantities separately. In this particular experiment, EOF-1 and EOF-2 capture 92%–97% and 2%–6% of the total variance, respectively; they reflect the combined effect of IWP and r_{eff}. EOF-3 only accounts for 1%–2% of the total variance and indicates $w(z)$ sensitivity. The differences in the percentages of variance are dependent on the range of values chosen for each quantity. The percent variance is only approximate because each EOF cannot be attributed to one physical quantity alone.

On the other hand, for the experiment with joint IWP and Z_{cld} variations, the EOFs are quite similar to those obtained by analyzing simulations with joint IWP, r_{eff}, and $w(z)$ variations. Likewise, the two leading EOFs from simulations that involve a range of IWP values alone are quite similar to EOFs for a collection of simulations with joint IWP and r_{eff} variations; still the shape of EOF-1 is modified by the presence of small r_{eff}, and the magnitude of variability in EOF-2 is sensitive to r_{eff}. Hence care must be taken when drawing conclusions about the physical quantity responsible for EOFs because different combinations of physical quantities can produce similar EOFs.

The suite of current and future high-resolution IR measurements will provide a wealth of radiance observations; there will help verify climate models over the years to come (Goody et al. 1998). One method of determining the reliability of GCM performance is by comparing EOFs of observed radiances with those calculated from model output. Our work diagnoses the radiance variability caused by a set of physical parameters

related to cirrus and attributes this variability to single or multiple physical quantities. Climate model verification uses comparisons of the overall difference between simulated and observed radiance spectra, as well as comparisons of radiance EOFs (Huang et al. 2002). Our work shows that the principal components (PCs) associated with some of these EOFs can be compared with the gridded physical fields simulated by GCMs (e.g., IWP, T_{sfc}, $w(z)$, etc.), both for climate and numerical weather prediction (NWP) models. Such a comparison is a powerful new tool for GCM validation.

In Part II, horizontal PC fields derived from AIRS spectra taken over cloudy scenes with cirrus will be compared to selected geophysical fields measured from independent data sources, for example, τ, r_{eff}, and $w(z)$ from the Moderate Resolution Imaging Spectroradiometer (MODIS; Platnick et al. 2003), and $T(z)$, T_{sfc}, and $w(z)$ from NWP models. By comparing the PC fields with these and other geophysical parameters, the uniqueness of particular EOFs to physical quantities can be explored.

The results of this work have quantified the sensitivity of IR spectra to cirrus cloud and atmospheric parameters. This information will be useful toward the development of a retrieval scheme for some of these geophysical parameters, specifically IWP (or τ) and r_{eff}. Since the EOFs of $T(z)$, Z_{cld}, ΔZ_{cld}, and IWP are similar to each other, the implication is that other sources of data besides IR radiances are needed to constrain the free parameters in the physical system. AIRS has the capability to retrieve $T(z)$ to 1-K absolute accuracy in 1-km layers, $w(z)$ to 20% in 2-km layers, Z_{cld} top to 0.5 km, and surface skin temperature to 1 K (Aumann et al. 2003), which can be used to constrain several of the free parameters. However, the accuracy of such quantities in the presence of extensive cloudiness is poorer (Susskind et al. 2003) and may need to be complemented with $T(z)$ and $w(z)$ from NWP models when encountering retrieval problems in some cloudy scenes. The Cloud-Aerosol Lidar and Infrared Pathfinder Satellite Observations (CALIPSO) will provide vertical cloud boundary information to an accuracy of 70 m, with the greatest sensitivity for thinner clouds. CloudSat (Stephens et al. 2002) uses a 94-GHz radar to detect cloud location at a vertical resolution of 500 m, which is more sensitive to thicker clouds than CALIPSO.

The A-train suite of instruments will provide an unprecedented opportunity for atmospheric and climate research. PCA will be an integral tool for the interpretation of this enormous and rich dataset.

REFERENCES

Ackerman, S. A., W. L. Smith, J. D. Spinhirne, and H. E. Revercomb, 1990: The 27–28 October 1986 FIRE IFO cirrus case study: Spectral properties of cirrus clouds in the 8–12 μm window. *Mon. Wea. Rev.,* **118,** 2377–2388.

——, ——, A. D. Collard, X. L. Ma, H. E. Revercomb, and R. O. Knuteson, 1995: Cirrus cloud properties derived from High Spectral Resolution Infrared Spectrometry during FIRE II. Part II: Aircraft HIS results. *J. Atmos. Sci.,* **52,** 4246–4263.

——, C. C. Moeller, K. I. Strabala, H. E. Gerber, L. E. Gumley, W. P. Menzel, and S. C. Tsay, 1998: Retrieval of effective microphysical properties of clouds: A wave cloud case study. *Geophys. Res. Lett.,* **25,** 1121–1124.

Aires, F., W. B. Rossow, N. A. Scott, and A. Chedin, 2002: Remote sensing from the Infrared Atmospheric Sounding Interferometer instrument—1. Compression, denoising, and first-guess retrieval algorithms. *J. Geophys. Res.,* **107,** 4619, doi:10.1029/2001JD000955.

Aumann, H. H., and Coauthors, 2003: AIRS/AMSU/HSB on the Aqua mission: Design, science objectives, data products, and processing systems. *IEEE Trans. Geosci. Remote Sens.,* **41,** 253–264.

Bantges, R. J., J. E. Russell, and J. D. Haigh, 1999: Cirrus cloud top-of-atmosphere radiance spectra in the thermal infrared. *J. Quant. Spectrosc. Radiat. Transfer,* **63,** 487–498.

Baran, A. J., S. Havemann, and D. Mackowski, 2002: A database of hexagonal column optical properties for wavelengths ranging between 0.2 μm to 30 μm. ANNEX 7, Contract 4b/3/ 02, DEFRA UK.

Beer, R., T. A. Glavich, and D. M. Rider, 2001: Tropospheric emission spectrometer for the Earth Observing System's Aura satellite. *Appl. Opt.,* **40,** 2356–2367.

Chung, S., S. A. Ackerman, P. F. van Delst, and W. P. Menzel, 2000: Model calculations and interferometer measurements of ice-cloud characteristics. *J. Appl. Meteor.,* **39,** 634–644.

Coakley, J. A., and F. P. Bretherton, 1982: Cloud cover from high-resolution scanner data: Detecting and allowing for partially filled fields of view. *J. Geophys. Res.,* **87,** 4917–4932.

Collard, A. D., S. A. Ackerman, W. L. Smith, X. Ma, H. E. Revercomb, R. O. Knuteson, and S.-C. Lee, 1995: Cirrus clouds properties derived from High Spectral Resolution Infrared Spectrometry during FIRE II. Part III: Ground-based HIS results. *J. Atmos. Sci.,* **52,** 4264–4275.

Conrath, B. J., R. A. Hanel, V. G. Kunde, and C. Prabhakara, 1970: The infrared interferometer experiment on Nimbus 3. *J. Geophys. Res.,* **75,** 5831–5857.

Cooper, S. J., T. S. L'Ecuyer, and G. L. Stephens, 2003: The impact of explicit cloud boundary information on ice cloud microphysical property retrievals from infrared radiances. *J. Geophys. Res.,* **108,** 4107, doi:10.1029/2002JD002611.

Cunningham, J. D., J. M. Haas, and H. Swenson, 2001: NPOESS instruments: The future of METSAT observations. Preprints, *11th Conf. on Satellite Meteorology and Oceanography,* Madison, WI, Amer. Meteor. Soc., P5.2.

Duda, D. P., J. D. Spinhirne, and W. D. Hart, 1998: Retrieval of contrail microphysical properties during SUCCESS by the split-window method. *Geophys. Res. Lett.,* **25,** 1149–1152.

Fu, Q., and K. N. Liou, 1993: Parameterization of the radiative properties of cirrus clouds. *J. Atmos. Sci.,* **50,** 2008–2025.

——, and W. Sun, 2001: Retrieval of cirrus particle sizes using a

split-window technique: A sensitivity study. *J. Quant. Spectrosc. Radiat. Transfer,* **70,** 725–736.

Goldberg, M. D., Y. Qu, L. M. McMillin, W. Wolf, L. Zhou, and M. Divakarla, 2003: AIRS near-real-time products and algorithms in support of operational numerical weather prediction. *IEEE Trans. Geosci. Remote Sens.,* **41,** 379–389.

Goody, R., J. Anderson, and G. North, 1998: Testing climate models: An approach. *Bull. Amer. Meteor. Soc.,* **79,** 2541–2549.

Hanel, R. A., B. J. Conrath, V. G. Kunde, C. Prabhakara, I. Revah, V. V. Salomonson, and G. Wolford, 1972: The Nimbus 4 infrared spectroscopy experiment 1. Calibrated thermal emission spectra. *J. Geophys. Res.,* **77,** 2629–2641.

Hansen, J. E., and L. D. Travis, 1974: Light scattering in planetary atmospheres. *Space Sci. Rev.,* **16,** 527–610.

Haskins, R., R. M. Goody, and L. Chen, 1997: A statistical method for testing a general circulation model with spectrally resolved satellite data. *J. Geophys. Res.,* **102,** 16 563–16 581.

——, ——, and ——, 1999: Radiance covariance and climate models. *J. Climate,* **12,** 1409–1422.

Henyey, L. G., and J. L. Greenstein, 1941: Diffuse radiation in the galaxy. *Astrophys. J.,* **93,** 70–83.

Houghton, J. T., Y. Ding, D. J. Griggs, M. Noguer, P. J. Van der Linden, and D. Xiaosu, Eds., 2001: *Climate Change 2001: The Scientific Basis.* Cambridge University Press, 944 pp.

Huang, H. L., and P. Antonelli, 2001: Application of principal component analysis to high-resolution infrared measurement compression and retrieval. *J. Appl. Meteor.,* **40,** 365–388.

Huang, X., J. Farrara, S. S. Leroy, Y. L. Yung, and R. M. Goody, 2002: Cloud variability as revealed in outgoing infrared spectra: Comparing model to observation with spectral EOF analysis. *Geophys. Res. Lett.,* **29,** 1270, doi:10.1029/2001GL014176.

Inoue, T., 1985: On the temperature and effective emissivity determination of semitransparent cirrus clouds by bi-spectral measurements in the 10 μm window region. *J. Meteor. Soc. Japan,* **63,** 88–98.

——, 1987: A cloud type classification with NOAA 7 split-window measurements. *J. Geophys. Res.,* **92,** 3991–4000.

Kahn, B. H., and Coauthors, 2003: Near micron-sized cirrus cloud particles in high-resolution infrared spectra: An orographic case study. *Geophys. Res. Lett.,* **30,** 1441, doi:10.1029/2003GL016909.

Lin, X., and J. A. Coakley Jr., 1993: Retrieval of properties for semitransparent clouds from multispectral infrared imagery data. *J. Geophys. Res.,* **98,** 18 501–18 514.

Liou, K. N., 2002: *An Introduction to Atmospheric Radiation.* Academic Press, 583 pp.

——, and Y. Takano, 1994: Light scattering by nonspherical particles: Remote sensing and climatic implications. *Atmos. Res.,* **31,** 271–298.

Luo, G., X. Lin, and J. A. Coakley Jr., 1994: 11-μm emissivities and droplet radii for marine stratocumulus. *J. Geophys. Res.,* **99,** 3685–3698.

Massie, S. T., and A. Goldman, 2003: The infrared absorption cross-section and refractive-index data in HITRAN. *J. Quant. Spectrosc. Radiat. Transfer,* **82,** 413–428.

McFarquhar, G. M., and A. J. Heymsfield, 1998: The definition and significance of an effective radius for ice clouds. *J. Atmos. Sci.,* **55,** 2039–2052.

Mishchenko, M. I., and L. D. Travis, 1998: Capabilities and limitations of a current Fortran implementation of the *T*-matrix method for randomly oriented, rotationally symmetric scatterers. *J. Quant. Spectrosc. Radiat. Transfer,* **60,** 309–324.

——, ——, and A. Macke, 1996: Scattering of light by polydisperse, randomly oriented, finite circular cylinders. *Appl. Opt.,* **35,** 4927–4940.

Moncet, J. L., and S. A. Clough, 1997: Accelerated monochromatic radiative transfer for scattering atmospheres: Application of a new model to spectral radiance observations. *J. Geophys. Res.,* **102,** 21 853–21 866.

Norton, R. H., and R. Beer, 1976: New apodizing functions for Fourier spectrometry. *J. Opt. Soc. Amer.,* **66,** 259–264.

Parol, F., J. C. Buriez, G. Brogniez, and Y. Fouquart, 1991: Information content of AVHRR channels 4 and 5 with respect to the effective radius of cirrus cloud particles. *J. Appl. Meteor.,* **30,** 973–984.

Platnick, S., M. D. King, S. A. Ackerman, W. P. Menzel, B. A. Baum, J. C. Riedl, and R. A. Frey, 2003: The MODIS cloud products: Algorithms and examples from Terra. *IEEE Trans. Geosci. Remote Sens.,* **41,** 459–473.

Platt, C. M. R., and Harshvardhan, 1988: Temperature dependence of cirrus extinction: Implications for climate feedback. *J. Geophys. Res.,* **93,** 11 051–11 058.

Prabhakara, C., R. S. Fraser, G. Dalu, M.-L. C. Wu, and R. J. Curran, 1988: Thin cirrus clouds: Seasonal distribution over oceans deduced from Nimbus-4 IRIS. *J. Appl. Meteor.,* **27,** 379–399.

——, J.-M. Yoo, G. Dalu, and R. S. Fraser, 1990: Deep optically thin cirrus clouds in the polar regions. Part I: Infrared extinction characteristics. *J. Appl. Meteor.,* **29,** 1313–1329.

——, D. P. Kratz, J.-M. Yoo, G. Dalu, and A. Vernekar, 1993: Optically thin cirrus clouds: Radiative impact on the warm pool. *J. Quant. Spectrosc. Radiat. Transfer,* **49,** 467–483.

Preisendorfer, R. W., 1988: *Principal Component Analysis in Meteorology and Oceanography.* Elsevier, 425 pp.

Press, W. H., S. A. Teukolsky, W. T., Vetterling, and B. P., Flannery, 1992: *Numerical Recipes in C: The Art of Scientific Computing.* Cambridge University Press, 1020 pp.

Rathke, C., and J. Fischer, 2000: Retrieval of cloud microphysical properties from thermal infrared observations by a fast iterative radiance fitting method. *J. Atmos. Oceanic Technol.,* **17,** 1509–1524.

Revercomb, H. E., H. Buijs, H. B. Howell, D. D. LaPorte, W. L. Smith, and L. A. Sromovsky, 1988: Radiometric calibration of IR Fourier transform spectrometers: Resolution to a problem with the High-Resolution Interferometer Sounder. *Appl. Opt.,* **27,** 3210–3218.

Simeoni, D., and C. Singer, 1997: Infrared Atmospheric Sounding Interferometer. *Acta Astronaut.,* **40,** 2–8.

Smith, W. L., and H. M. Woolf, 1976: Use of eigenvectors of statistical covariance matrices for interpreting satellite sounder radiometer observations. *J. Atmos. Sci.,* **33,** 1127–1140.

——, H. E. Revercomb, R. O. Knuteson, F. A. Best, R. Dedecker, H. B. Howell, and H. M. Woolf, 1995: Cirrus cloud properties derived from high spectral resolution infrared spectrometry during FIRE II. Part I: The High Resolution Interferometer Sounder (HIS) systems. *J. Atmos. Sci.,* **52,** 4238–4245.

——, S. A. Ackerman, H. Revercomb, H. Huang, D. H. DeSlover, W. Feltz, L. Gumley, and A. Collard, 1998: Infrared spectral absorption of nearly invisible cirrus. *Geophys. Res. Lett.,* **25,** 1137–1140.

Stephens, G. L., 2002: Cirrus, climate, and global change. *Cirrus,* D. K. Lynch et al., Eds., Oxford University Press, 433–448.

——, S.-C. Tsay, P. W. Stackhouse Jr., and P. J. Flatau, 1990: The relevance of the microphysical and radiative properties of cirrus clouds to climate and climatic feedback. *J. Atmos. Sci.,* **47,** 1742–1753.

——, and Coauthors, 2002b: The CloudSat mission and the A-train. *Bull. Amer. Meteor. Soc.,* **83,** 1771–1790.

Strabala, K. I., and S. A. Ackerman, 1994: Cloud properties inferred from 8–12-μm data. *J. Appl. Meteor.,* **33,** 212–229.

Susskind, J., C. D. Barnet, and J. M. Blaisdell, 2003: Retrieval of atmospheric and surface parameters from AIRS/AMSU/HSB data in the presence of clouds. *IEEE Trans. Geosci. Remote Sens.,* **44,** 390–409.

Toon, O. B., M. A. Tolbert, B. G. Koehler, A. M. Middlebrook, and J. Jordan, 1994: Infrared optical constants of H_2O ice, amorphous nitric acid solutions, and nitric acid hydrates. *J. Geophys. Res.,* **99,** 25 631–25 654.

Wilks, D. S., 1995: *Statistical Methods in the Atmospheric Sciences.* Academic Press, 467 pp.

Wu, M.-L., 1987: A method for remote sensing the emissivity, fractional cloud cover and cloud top temperature of high-level, thin clouds. *J. Climate Appl. Meteor.,* **26,** 225–233.

Xu, L., J. Ding, and A. Y. S. Chang, 2002: Scattering matrix of infrared radiation by ice finite circular cylinders. *Appl. Opt.,* **41,** 2333–2348.

Yang, P., H. L. Wei, B. A. Baum, H. L. Huang, A. J. Heymsfield, Y. X. Hu, B. C. Gao, and D. D. Turner, 2003: The spectral signature of mixed phase clouds composed of nonspherical ice crystals and spherical liquid droplets in the terrestrial window region. *J. Quant. Spectrosc. Radiat. Transfer,* **79,** 1171–1188.